Haibao Zhang, Tengfei Cao and Yi Cheng*

Synthesis of nanostructured MgO powders with photoluminescence by plasma-intensified pyrohydrolysis process of bischofite from brine

Abstract: Nanostructured MgO powders were synthesized by an ultra-high temperature pyrohydrolysis process of bischofite ($MgCl_2 \cdot 6H_2O$) in a radio frequency (RF) induction thermal plasma system. The structure, morphology and optical properties were characterized by X-ray diffraction (XRD), energy-dispersive X-ray spectroscopy (EDS), scanning electron microscopy (SEM), transmission electron microscopy (TEM) and Raman spectroscopy. The results showed that MgO nanopowders with two different morphologies were fabricated: near spherical MgO nanoparticles with size in the range of 20~40 nm and 1D nanobelts with a width of about 100 nm. The photoluminescence (PL) studies showed that both of these two kinds of nanostructured MgO powders exhibited a strong ultraviolet-green PL emission under the excitation of 325 nm He-Ne laser.

Keywords: MgO nanopowder; photoluminescence; process intensification; synthesis; thermal plasma.

***Corresponding author: Yi Cheng,** Department of Chemical Engineering, Tsinghua University, Beijing 100084, PR China, e-mail: yicheng@tsinghua.edu.cn
Haibao Zhang and Tengfei Cao: Department of Chemical Engineering, Tsinghua University, Beijing 100084, PR China

1 Introduction

Nanostructured MgO products have been receiving more and more attention due to their promising applications in heterogeneous catalysis [1–3], catalyst support [4, 5] and environmental toxins adsorption [6–8]. As a result, extensive research has been focused on the fabrication of nanostructured MgO products [9–11]. For example, Montero et al. [2] synthesized nano MgO contained well-defined cubic MgO nanocrystallites through the solvothermal high temperature process. Glaspell et al. [4] fabricated MgO nanocubes which supported Au and Pd nanoparticle catalysts for CO oxidation. Liu et al. [12] prepared the mesoporous carbon stabilized MgO nanoparticles by fast pyrolysis of $MgCl_2$ loaded biomass for CO_2 capture. Zhu et al. [13, 14] developed a procedure to generate MgO (111) nanosheets with a thickness typically between 3 and 5 nm via a facile wet chemical process. Maliyekkal et al. [15] adopted self-propagated combustion of the magnesium nitrate trapped in cellulose fibers for synthesis of nanoparticles. It seems that some harsh or complicated conditions are necessary to tailor synthesis, for example, high temperature or pressure, several experiment steps and complicated reagents like organic magnesium compounds $Mg(OCH_3)_2$ or $Mg(CH_3COO)_2.2H_2O$. The main disadvantages of these methods are the relatively low production rate, high material or energy consumption and difficulties in obtaining the MgO nanoparticles with the desired purity and particle size distribution in a continuous and scalable process.

Traditionally, MgO powder was prepared through a high temperature pyrolysis method using the magnesium salt or magnesium hydroxide, sometimes salt lake brine directly, as the raw material. As liquid mines, salt lakes are important natural assets which are often used to extract numerous valuable chemicals. However, the magnesium brines or bischofite ($MgCl_2 \cdot 6H_2O$) resulting from the mining process of salt lakes often cannot be utilized effectively and are discarded back into the salt lakes [16]. This has caused the waste of valuable magnesium resources. At the same time, the ecosystem and surrounding environment of the salt lakes have been changed and threatened by the wasted brine. Therefore, utilization of magnesium resources existing in the salt lakes has significantly technological, economic and environmental benefits. Early in the 1960s, Dead Sea Periclase Ltd. (DSP) utilized the high temperature pyrohydrolysis method named as the "Aman process" for value-added conversion of bischofite from brine to high purity MgO directly [17]. However, the particle size of the product obtained from the "Aman process" was in the range of 70~90 μm. At the same time, because of the difficulty of the dehydration of bischofite, a high temperature commonly up to ~2000 K is maintained for preparation of high purity MgO. This makes this process energy-intensive, and the setup is easy to be corroded in the high temperature hydrochloric acid atmosphere.

In the past 30 years, thermal plasmas at atmospheric pressure have been used more extensively for process intensification and materials synthesis, such as the pyrolysis of chemicals and fabrication of nanomaterials [18–21]. Among various kinds of thermal plasmas, radio frequency (RF) induction thermal plasma is used commonly, which offers longer residence/reaction times by virtue of larger volume and lower velocities [22]. Furthermore, RF induction thermal plasma is very suitable for synthesis of high purity products, due to the absence of electrodes from the plasma system [23–26]. In a typical RF induction thermal plasma system, the temperature (>3000 K) allows for the decomposition of nearly arbitrary precursors [27]. To the best of our knowledge, little work has been focused on the synthesis of nanostructured MgO powders via RF induction thermal plasma enhanced pyrohydrolysis of bischofite from waste brine. Therefore, this technological route is still a formidable challenge.

Herein, we present an approach of bischofite pyrohydrolysis enhanced by RF induction thermal plasma. $MgCl_2 \cdot 6H_2O$ aqueous solution is employed as a precursor and is converted to value-added high purity MgO nanopowders. In addition, we optimize the process parameters in order to study the pyrohydrolysis characteristics of $MgCl_2 \cdot 6H_2O$ aqueous solutions.

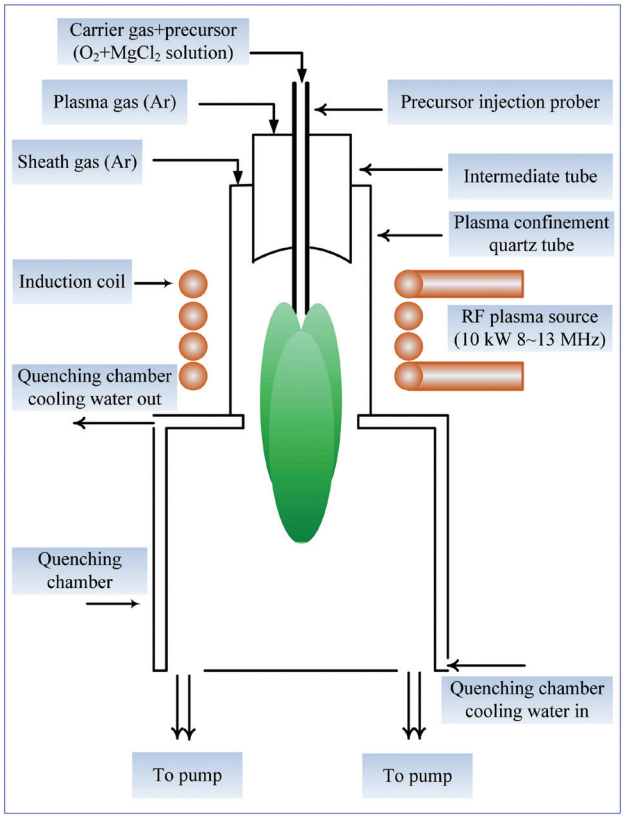

Figure 1 Schematic diagram of the radio frequency (RF) induction thermal plasma system.

2 Materials and methods

The pyrohydrolysis of $MgCl_2 \cdot 6H_2O$ aqueous solution was carried out in a homemade RF induction thermal plasma system at atmospheric pressure. The schematic diagram of the setup is shown in Figure 1. The system mainly consists of an RF generator, a plasma torch, a quenching chamber, a gas delivery system, a precursor feeding system and an off-gas exhaust system. The excitation frequency of the RF plasma source is 8~13 MHz and the working power is 10 kW. The working power of the RF thermal plasma setup was fixed at 10 kW for the continuous and stable operation of plasma. The RF induction thermal plasma torch comprises three major parts: a four-turn water-cooled induction copper coil, a confinement tube and a water-cooled precursor injection probe. Three gas streams, i.e., a central gas, a protective sheath gas and a feedstock carrier gas, are injected through the RF induction thermal plasma torch. The central gas, also known as the plasma gas, is injected into the confinement tube continually to stabilize the plasma jet. The sheath gas is injected tangentially to protect the torch wall from being damaged due to the high temperature of the thermal plasma. RF induction thermal plasma is generated by electrodeless discharges, in which the RF electrical energy in a copper coil is coupled to a plasma gas by eddy currents through magnetic induction. The raw materials are introduced axially into the plasma jet through the water-cooled probe located at the center of the plasma torch. This injection scheme allows for the delivery of the raw materials directly into the high temperature core region of the plasma jet. The reaction part is a vertical quartz tube of 4 cm inner diameter and 20 cm length. The quenching chamber connected to the bottom of the reactor is a water-cooled two-layer stainless-steel box. The high pressure constant flow pump is used to feed the $MgCl_2$ solution with a controlled flow rate into the plasma zone.

$MgCl_2 \cdot 6H_2O$ (98%, Beijing Chemical Plant) was used as received without further purification. A saturated $MgCl_2$ solution with a concentration of 740 g/l was prepared by dissolving the $MgCl_2 \cdot 6H_2O$ into de-ionized water. Argon was employed as the plasma gas. The precursor solution was fed via a water-cooled atomizer probe into the plasma zone with the oxygen flow. Reaction products were collected on the inner wall of the plasma reactor. For stable operation of the RF thermal plasma, the parameters for

plasma processing are of vital importance. The detailed operation parameters of the plasma deposition process are given in Table 1.

In order to purify the pyrohydrolysis raw product, additional posttreatment has to be conducted. The powders obtained were mixed with de-ionized water and stirred for 30 min to convert all MgO to insoluble $Mg(OH)_2$. Meanwhile, the residual salts (sodium, potassium, chlorine, etc.) were dissolved and can be readily separated from the $Mg(OH)_2$ by the following filtration and washing procedures. The washing stage was monitored by chloride removal efficiency. The chloride content of the eluate was measured by an $AgNO_3$ indicator. Subsequent drying and calcining of the residue were conducted at 378 K and 1173 K, respectively, to obtain high purity MgO.

The microstructures of the samples were analyzed by an X-ray powder diffractometer (XRD, D8-Advance, Bruker, Germany) using Cu Kα radiation (λ=1.54178 Å) at a fixed power source (40.0 kV, 40.0 mA). Field emission scanning electron microscopy (FESEM, JSM-7401F, JEOL, Japan) equipped with an energy-dispersive X-ray spectrometer (EDS) was used to characterize the morphologies and elemental compositions of the samples. Prior to the measurements, the samples were coated with a thin gold film by means of vacuum sputtering, to improve electrical conductivity. High-resolution transmission electron microscopy (HRTEM, JEM-2010, JEOL, Japan and 120.0 kV) was also used to characterize the morphologies and the microstructures of the samples. To prepare specimens for TEM, the powders were mixed with absolute alcohol, ultrasonically dispersed for 20 min, and then dropped onto the carbon-coated copper grids. The grain sizes of the synthesized products were calculated from the XRD pattern using the Scherrer equation. A BET surface area analyzer (Micrometric, ASAP 2010) was used to measure the average size of the produced MgO particles. Photoluminescence (PL) measurements were carried out at room temperature using a 325 nm line of a He-Ne laser as the excitation source, with micro Raman spectroscopy (Horibra LABRAM-HR).

Table 1 Parameters of the thermal plasma deposition process.

Parameters	Values
Plasma power (kW)	10
Central gas, argon (m^3/h)	0.2
Sheath gas, argon (m^3/h)	4
Carrier gas, oxygen (m^3/h)	0.4
Feeding rate (ml/min)	0.30, 0.60, 0.90, 1.20, 1.50

3 Results and discussion

3.1 Compositional characterization

The color of the plasma flame is determined by the atomic and molecular species excited to emit lights. In this work, the MgO deposited on the inside wall of the quartz tube is excited by the UV light produced by the $Ar+O_2$ plasma and then re-emits green light [28]. All of the products obtained under various conditions are white powders.

It is a very important step to inject the liquid precursors into the plasma system. The atomization of the liquid precursor and the continuity of feeding are two key factors concerned in a specific pyrolysis experiment which could affect the stability of plasma discharge, the efficiency of pyrolysis and the homogeneity of products. These two key factors are determined by the flow rate of the carrier gas and the feeding rate of the liquid precursor. In this work, the flow rate of carrier gas (O_2) was controlled at 0.4 m^3/h to ensure the liquid precursor atomized and dispersed uniformly. By optimizing the operating conditions, the efficiency of plasma pyrolysis was investigated at the feeding rate of liquid precursor at 0.3~1.5 ml/min. Figure 2 shows the XRD patterns of the raw products obtained at different precursor feeding rates. The main peaks match well with Bragg reflection of the standard cubic phase MgO (JCPDS No.00-003-0998, space group: Fm-3m, lattice constants: a=b=c=4.2030 Å, and α=β=90°). This indicates that these products are composed mainly of cubic phase MgO. At the

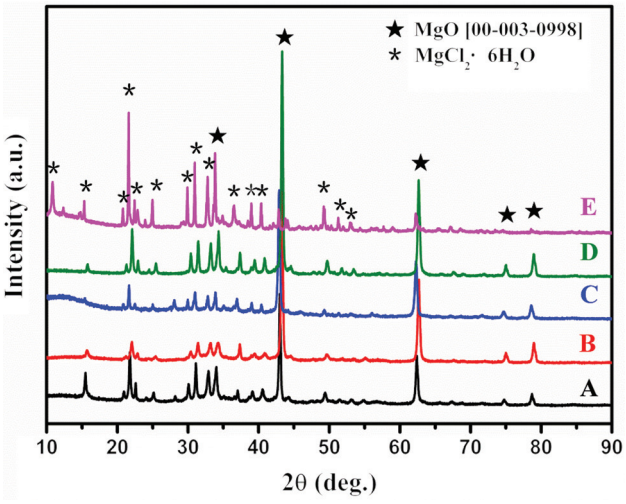

Figure 2 X-ray diffraction (XRD) patterns of the products synthesized by the radio frequency (RF) induction thermal plasma process with different precursor feeding rates: (A) 0.30 ml/min; (B) 0.60 ml/min; (C) 0.90 ml/min; (D) 1.20 ml/min; and (E) 1.50 ml/min. (The numbers after the phases are the JCPDS file numbers.)

same time, some small peaks traceable to $MgCl_2 \cdot 6H_2O$ are observed in the XRD patterns. The residual $MgCl_2 \cdot 6H_2O$ may be attributed to the following reasons. Firstly, the precursor is decomposed to Mg^{2+} and Cl^-, however, the ions Mg^{2+}, Cl^- and H_2O recombined in the low temperature zone. Secondly, the precursor injected into the high temperature plasma flame may be too much to be decomposed completely and could deliquesce back to the hexahydrate state during the collection and characterization process. This is proved by the XRD patterns in which no peaks of lower hydrate compounds can be found, and the most peaks due to $MgCl_2 \cdot 6H_2O$ appear at the largest precursor feeding rate concerned in this experiment, as shown in Figure 2E.

Although the products obtained from the pyrohydrolysis of $MgCl_2$ solution in RF induction thermal plasma contain $MgCl_2 \cdot 6H_2O$, the residues can be tolerated because they can be fully reduced during the subsequent posttreatment process. After posttreatment, no characteristic peaks of impurities, such as $MgCl_2 \cdot 6H_2O$ and $MgCl_2$, can be observed, as shown in Figure 3B; this indicates that the product has high purity. The yield of the product is 64.84% during the calcination stage, approaching the theory value, 68.97%, of $Mg(OH)_2$ decomposition to MgO. Therefore, we estimate that almost all MgO produced from pyrohydrolysis has converted to $Mg(OH)_2$ in the posttreatment stage. It means that the mentioned plasma pyrohydrolysis process of bischofite from brine could also be used for high purity $Mg(OH)_2$ production.

Figure 4 presents corresponding EDS spectra of the products before and after posttreatment. The main

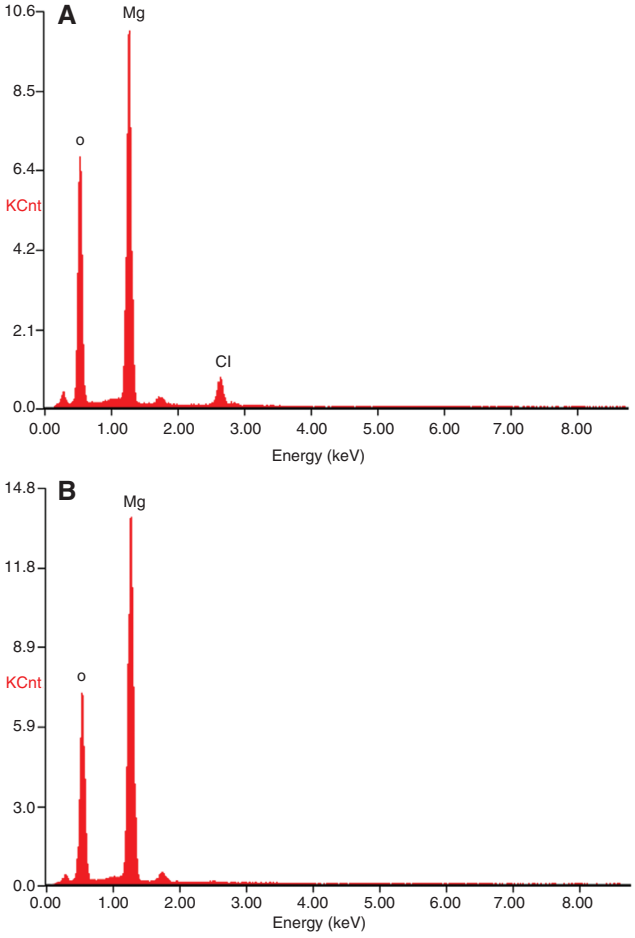

Figure 4 Typical EDS spectra of the products obtained by thermal plasma process: (A) before treatment with feeding rate of 1.50 ml/min; and (B) its corresponding product after posttreatment.

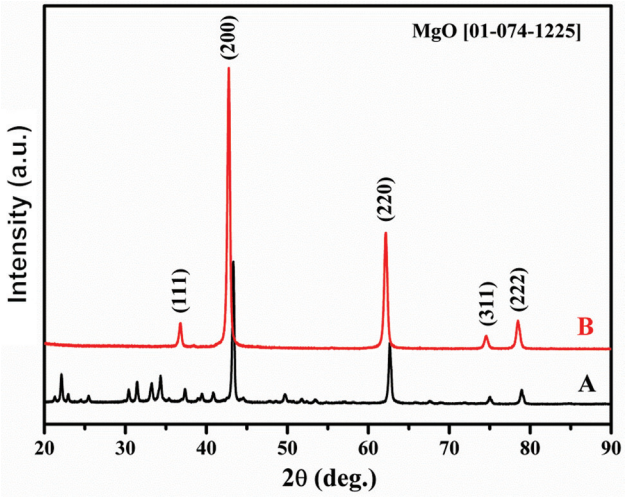

Figure 3 Typical X-ray diffraction (XRD) patterns of the products obtained by thermal plasma process: (A) before treatment with feeding rate of 1.50 ml/min; and (B) its corresponding product after posttreatment. (The numbers after the phases are the JCPDS file numbers.)

superficial elements of the raw product are O, Mg and Cl (minor C detected due to the C-containing conductive glue used in mounting the samples in SEM not being labeled), as shown in Figure 4A. This indicates the residual of $MgCl_2/MgCl_2 \cdot 6H_2O$ in the raw products. However, water-soluble salts in raw products can be removed through the subsequent washing operation. The EDS spectrum of the final products shows the absence of Cl after posttreatment and only O and Mg are detected, as shown in Figure 4B. The EDS analysis results agree well with the XRD patterns shown in Figure 3.

Similar to the "Aman process", the thermal plasma process needs no additional raw materials other than energy and $MgCl_2$ brine during the pyrohydrolysis and posttreatment stages. Therefore, the products are free of the impurities presented in conventional wet chemical processes, in which lime or dolomite is reacted as a precipitator with $MgCl_2$ solution.

However, the high temperature heat sources of the two processes differ from each other. Hot gases or steam obtained by the combustion of fuels are injected into the Aman reactor. Commonly, the temperature in the Aman reactor is maintained at ~1000 K for a long time. And $MgCl_2$ brine is thermally decomposed to raw MgO. The RF induction thermal plasma sustained by inductive coupling of energy from the oscillator circuit can reach local thermodynamic equilibrium in milliseconds. The temperature of the steady-state thermal plasma is in the range of 3000~10,000 K. The residence time of raw materials in the plasma is only several ms [29]. The ms, ultra-high temperature pyrohydrolysis process in the thermal plasma has much higher reaction efficiency than the "Aman process".

Moreover, the Aman furnace is complex and easily corroded by the hydrochloric acid gas at high temperatures. The thermal plasma flame has the characteristic of a high quenching rate (10^5~10^6 K/s). With the help of ms time reaction and quenching characteristics, the thermal plasma process could protect and simplify the plasma equipment efficiently. At this point, we could find many researches and applications of thermal plasmas in hydrochloric acid gas involved processes in recent years [30–32].

3.2 Morphological characterization and growth mechanism

The decomposition of the precursor in thermal plasma mainly takes place in the high temperature flame zone. However, the rapid quenching rate will lower the temperature of the plasma flame tail and enhance the degree of supersaturation of the vapor species. Homogeneous nucleation completes immediately through physical vapor deposition under high supersaturation conditions. The temperature gradient and flow field in the plasma system are of vital importance, and determine the properties including morphology, particle size and distribution of the final products. Figure 5A and B show typical SEM images of the as-prepared MgO powders collected from different positions of the plasma system. Corresponding TEM images are shown in Figure 5C and D, respectively. Products collected from the discharge quartz tube are near spherical nanoparticles with the size of 20~40 nm, as shown in Figure 5C. This may be attributed to the relatively high supersaturation and high temperature around the plasma jet that contributed to the isotropic growth, as shown in Figure 6. The narrow distribution of the particle

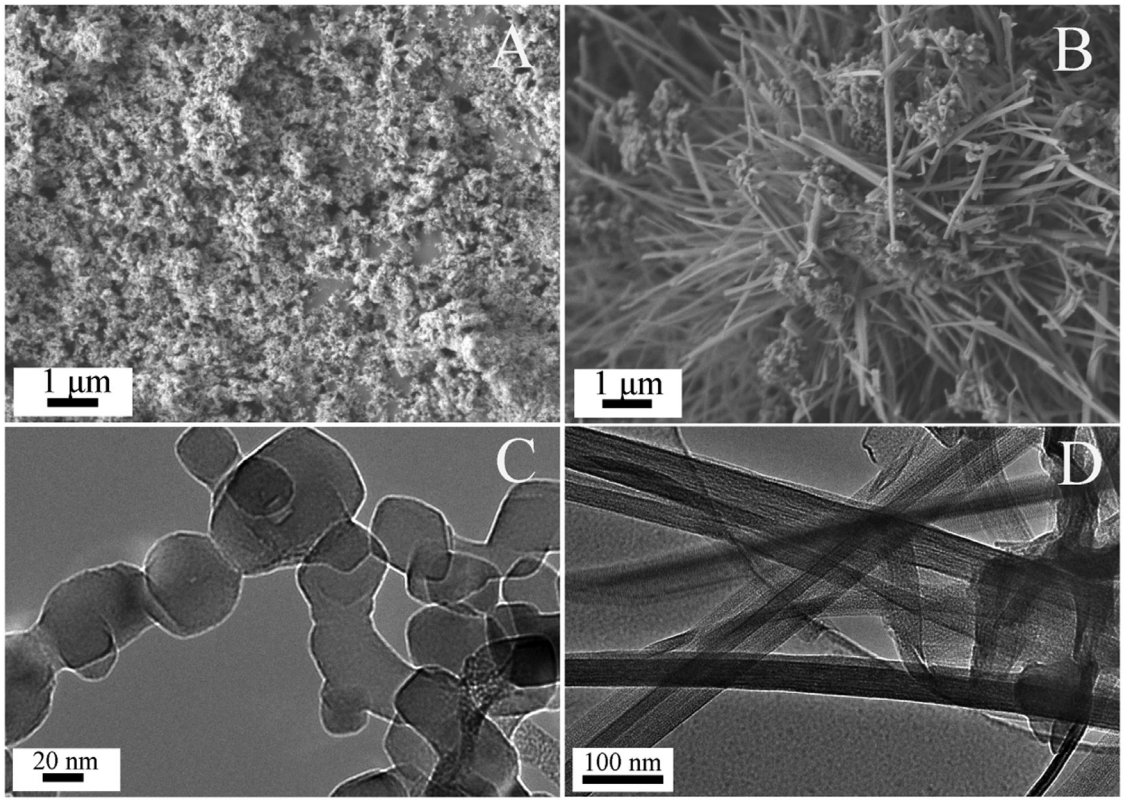

Figure 5 Typical scanning electron microscopy (SEM) images of the product synthesized from different positions of the plasma system: the discharge quartz tube (A) and the quenching chamber (B), corresponding transmission electron microscopy (TEM) images (C) and (D).

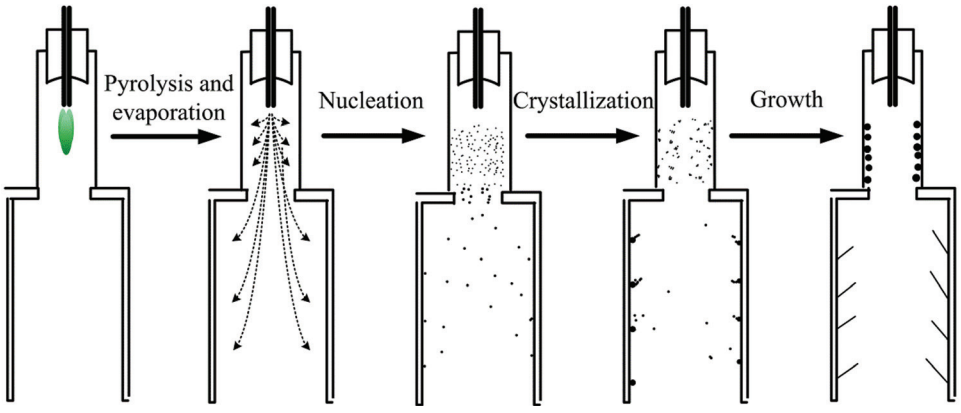

Figure 6 Growth mechanism of nanostructured MgO powders in the radio frequency (RF) thermal plasma system.

sizes strongly suggests that product particles are nucleated by purely homogeneous processes. In contrast with spherical nanoparticles, 1D MgO nanobelts with a width of about 100 nm were obtained from the quenching chamber of the plasma system, as shown in Figure 5B and D. The relatively low gas phase supersaturation and temperature in the quenching chamber drive the epitaxial nucleation and growth [33]. Thus, we can control the morphology of the nanosized MgO products through promoting the temperature gradient and flow field in the plasma system.

3.3 PL property

Optical properties are important for understanding the structure of materials. They also promote the possibility of extending the potential application of materials in optoelectronic devices. The PL property is very sensitive to the surface site information and the microstructure of materials. In recent years, there have been a considerable number of reports about the PL property of MgO [34–37]. However, the emission spectra of MgO reported were not in accordance with each other. In the present work, the PL properties of nanostructured MgO products are investigated in an excitation wavelength of 325 nm (3.82 eV). Figure 7 gives the emission spectra of as-prepared MgO products and indicates that the main emission peaks locate at ~350 (3.54 eV), ~380 (3.27 eV), and ~500 nm (2.48 eV). Therefore, the PL spectra of the two kinds of samples mainly consist of three bands: two UV bands centered at ~350 (3.54 eV) and ~380 (3.27 eV) and a green band centered at ~500 nm (2.48 eV). MgO, with a band gap of 7.8 eV, is often used as a prototypical ionic insulator. Therefore, it is obvious that the maximum band gap between 2.5~5.0 eV of MgO nanoparticles is not the intrinsic band gap of MgO. These emissions are attributed to various structural

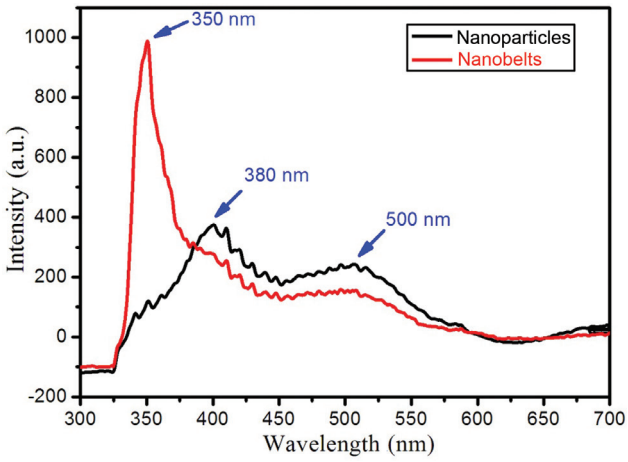

Figure 7 Photoluminescence (PL) spectra of two kinds of nanostructured MgO products synthesized by the radio frequency (RF) induction thermal plasma process.

defects. The optical properties of MgO were explained on the basis of F centers and/or charge transfer occurring at low coordination number sites [38, 39]. The emission bands centered at around 350 nm and 380 nm are attributed to low-coordinate oxide ions present at terrace sites (O_{5C}^{2-}) and edge sites (O_{4C}^{2-}), respectively [40, 41]. The broadened green emission band centered at ~500 nm is attributed to the presence of defects (F centers) related to oxygen ion vacancies [42].

4 Conclusion

With the process intensification of RF induction thermal plasma, bischofite has been pyrohydrolysized and efficiently converted to value-added high purity nanostructured MgO powders. The results show that two kinds of

high purity nanostructured MgO products can be fabricated: high purity spherical MgO nanoparticles with a size in the range of 20~40 nm and 1D MgO nanobelts with a width of about 100 nm. The PL property studies show that these two kinds of nanostructured MgO powders exhibit strong ultraviolet-green PL emission under the excitation of a 325 nm He-Ne laser. Compared with other conventional processes, the RF induction thermal plasma process has shown considerable promise for the direct pyrohydrolysis of $MgCl_2$ solution without any other external raw materials. Owing to the ultra-high temperature generated by the thermal plasma flame, the $MgCl_2$ solution was volatilized and pyrohydrolysized rapidly and successfully converted to high purity nanosized MgO powders with special morphology. In addition, these materials can undergo further processing to yield a wide range of value-added products that are differentiated by their physical properties such as particle size, bulk density, reactivity and surface area. So, the RF induction thermal plasma method not only enables value-added conversion of bischofite from brine, but is also more conducive to promote the comprehensive utilization of resources and the sustainable development of the environment of salt lakes.

Acknowledgments: This study is supported by the National Basic Research Program of China (973 Program no. 2012CB720301), the National Natural Science Foundation of China (NSFC) under grant no. 21176137.

Received March 21, 2014; accepted April 11, 2014

References

[1] Sundarrajan S, Chandrasekaran AR, Ramakrishna S. *J. Am. Ceram. Soc.* 2010, 93, 3955–3975.
[2] Montero JM, Brown DR, Gai PL, Lee AF, Wilson K. *Chem. Eng. J.* 2010, 161, 332–339.
[3] Verziu M, Cojocaru B, Hu JC, Richards R, Ciuculescu C, Filip P, Parvulescu VI. *Green Chem.* 2008, 10, 373–381.
[4] Glaspell G, Hassan HMA, Elzatahry A, Fuoco L, Radwan NRE, El-Shall MS. *J. Phys. Chem. B* 2006, 110, 21387–21393.
[5] Rakmak N, Wiyaratn W, Bunyakan C, Chungsiriporn J. *Chem. Eng. J.* 2010, 162, 84–90.
[6] Yu X, Luo T, Jia Y, Zhang Y, Liu J, Huang X. *J. Phys. Chem. C.* 2011, 115, 22242–22250.
[7] Hu J, Song Z, Chen L, Yang H, Li J, Richards R. *J. Chem. Eng. Data* 2010, 55, 3742–3748.
[8] Moussavi G, Mahmoudi M. *J. Hazard. Mater.* 2009, 168, 806–812.
[9] Pashchanka M, Hoffmann RC, Schneider JJ. *J. Mater. Chem.* 2010, 20, 957–963.
[10] Rezaei M, Khajenoori M, Nematollahi B. *Powder Technol.* 2011, 205, 112–116.
[11] Montero JM, Gai P, Wilson K, Lee AF. *Green Chem.* 2009, 11, 265–268.
[12] Liu W, Jiang H, Tian K, Ding Y, Yu H. *Environ. Sci. Technol.* 2013, 47, 9397–9403.
[13] Zhu KK, Hu JC, Kubel C, Richards R. *Angew. Chem. Int. Ed.* 2006, 45, 7277–7281.
[14] Hu JC, Zhu K, Chen LF, Kubel C, Richards R. *J. Phys. Chem. C.* 2007, 111, 12038–12044.
[15] Maliyekkal SM, Antony A, Pradeep T. *Sci. Total Environ.* 2010, 408, 2273–2282.
[16] Wang JF, Li ZB. *Ind. Eng. Chem. Res.* 2012, 51, 7874–7883.
[17] Epstein JA. *Hydrometallurgy* 1976, 2, 1–10.
[18] Hessel V, Cravotto G, Fitzpatrick P, Patil BS, Lang J, Bonrath W. *Chem. Eng. Process.* 2013, 71, 19–30.
[19] Yan B, Lu W, Cheng Y. *Green Proc. Synth.* 2012, 1, 33–47.
[20] Zheng J, Yang R, Xie L, Qu JL, Liu Y, Li XG. *Adv. Mater.* 2010, 22, 1451–1473.
[21] Shigeta M, Murphy AB. *J. Phys. D Appl. Phys.* 2011, 44, 174025.
[22] Shigeta M, Watanabe T. *J. Phys. D Appl. Phys.* 2007, 40, 2407–2419.
[23] Boulos M. *Met. Powder Rep.* 2004, 59, 16–21.
[24] Ishigaki T, Li JG. *Pure Appl. Chem.* 2008, 80, 1971–1979.
[25] Li J, Kamiyama H, Wang X, Moriyoshi Y, Ishigaki T. *J. Eur. Ceram. Soc.* 2006, 26, 423–428.
[26] Zhang H, Yao M, Bai L, Xiang W, Jin H, Li J, Yuan F. *CrystEngComm* 2013, 15, 1432–1438.
[27] Zhang H, Bai L, Hu P, Yuan F, Li J. *Int. J. Refract. Met. H.* 2012, 31, 33–38.
[28] Hong YC, Uhm HS. *Chem. Phys. Lett.* 2006, 422, 174–178.
[29] Guo JY, Fan XB, Dolbec R, Xue SW, Jurewicz J, Boulos M. *Plasma Sci. Technol.* 2010, 12, 188–199.
[30] Zheng J, Yang R, Chen WM, Xie L, Li XG, Chen CP. *J. Phys. D Appl. Phys.* 2009, 42, 185209.
[31] Yang R, Zheng J, Li W, Qu JL, Li XG. *J. Phys. D Appl. Phys.* 2011, 44, 174015.
[32] Fazekas P, Bódis E, Keszler AM, Czégény Z, Klébert S, Károly Z, Lgyi JS. *Plasma Chem. Plasma Process.* 2013, 33, 765–778.
[33] Kong PC, Pfender E. *Langmuir* 1987, 3, 259–265.
[34] Stankic S, Muller M, Diwald O, Sterrer M, Knozinger E, Bernardi J. *Angew. Chem. Int. Ed.* 2005, 44, 4917–4920.
[35] Stankic S, Bernardi J, Diwald O, Knozinger E. *J. Phys. Chem. B* 2006, 110, 13866–13871.
[36] Benedetti S, Benia HM, Nilius N, Valeri S, Freund HJ. *Chem. Phys. Lett.* 2006, 430, 330–335.
[37] Al-Gaashani R, Radiman S, Al-Douri Y, Tabet N, Daud AR. *J. Alloys Compd.* 2012, 521, 71–76.
[38] Li H, Li M, Wang X, Wu X, Liu F, Yang B. *Mater. Lett.* 2013, 102, 80–82.

[39] Rosenblatt GH, Rowe MW, Williams GP, Williams RT, Chen Y. *Phys. Rev. B* 1989, 39, 10309–10318.
[40] Li MJ, Wang XF, Li HJ, Di HR, Wu XG, Fang CR, Yang BH. *Appl. Surf. Sci.* 2013, 274, 188–194.
[41] Sterrer M, Berger T, Diwald O, Knözinger E. *J. Am. Chem. Soc.* 2002, 125, 195–199.
[42] Janet CM, Viswanathan B, Viswanath RP, Varadarajan TK. *J. Phys. Chem. C.* 2007, 111, 10267–10272.

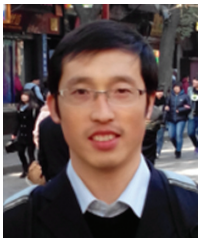

Haibao Zhang received his PhD degree in Chemical Engineering from the Institute of Process and Engineering (IPE), Chinese Academy of Science (CAS) in 2012. Afterwards, he worked as a postdoctor at Tsinghua University, China. He is experienced in thermal plasma process intensification and its application in value-added functional powder materials synthesis.

Tengfei Cao received his bachelor's degree from the Department of Chemical Engineering, Tsinghua University in 2010. Then, he started his PhD study in the same department, supervised by Professor Yi Cheng. He presently works on the atmospheric pressure thermal plasma enhanced chemical vapour deposistion (PECVD) of nanocrystalline silicon and silicon quantum dots with silicon tetrachloride as a precursor. He is also a co-worker in a project of the fabrication of high purity nanosized MgO powders.

Yi Cheng is a Professor in the Department of Chemical Engineering at Tsinghua University. He received his BSc in 1994 and his PhD in 2000, both from Tsinghua University. He then worked at Delft University of Technology and University of Western Ontario for years. Professor Cheng engages in the area of chemical reaction engineering, involving applications in clean fuel production, coal pyrolysis in thermal plasma, coal to synthetic natural gas (SNG), cold-plasma assisted material synthesis and catalysis, microreactor techniques for hydrogen production, chemicals and functional particle preparation.